

Journal of Materials Chemistry A

Accepted Manuscript



This is an *Accepted Manuscript*, which has been through the Royal Society of Chemistry peer review process and has been accepted for publication.

Accepted Manuscripts are published online shortly after acceptance, before technical editing, formatting and proof reading. Using this free service, authors can make their results available to the community, in citable form, before we publish the edited article. We will replace this *Accepted Manuscript* with the edited and formatted *Advance Article* as soon as it is available.

You can find more information about *Accepted Manuscripts* in the [Information for Authors](#).

Please note that technical editing may introduce minor changes to the text and/or graphics, which may alter content. The journal's standard [Terms & Conditions](#) and the [Ethical guidelines](#) still apply. In no event shall the Royal Society of Chemistry be held responsible for any errors or omissions in this *Accepted Manuscript* or any consequences arising from the use of any information it contains.

Cite this: DOI: 10.1039/coxx00000x

www.rsc.org/xxxxxx

ARTICLE TYPE

Towards High-Potential and Ultralong-life Cathodes for Sodium Ion Batteries: Freestanding 3D Hybrid Foams of $\text{Na}_7\text{V}_4(\text{P}_2\text{O}_7)_4(\text{PO}_4)$ and $\text{Na}_7\text{V}_3(\text{P}_2\text{O}_7)_4$ @Biomass-derived Porous Carbon

Qiufeng Li^{a,†}, Bo Lin^{b,†}, Sen Zhang^{*a}, Chao Deng^{*b}

Received (in XXX, XXX) Xth XXXXXXXXX 20XX, Accepted Xth XXXXXXXXX 20XX

DOI: 10.1039/b000000x

High-potential sodium hosts have attracted enormous attention recently in view of the requirement on improving energy density for sodium ion batteries. $\text{Na}_7\text{V}_4(\text{P}_2\text{O}_7)_4(\text{PO}_4)$ and $\text{Na}_7\text{V}_3(\text{P}_2\text{O}_7)_4$ with operating potentials near 4.0 V vs. Na^+/Na are promising cathode candidates. But the low conductivity, limited ion intercalation kinetics and inferior stability remain critical drawbacks for their practical applications. Herein, we report the design of freestanding 3D hybrid foams of high-potential sodium hosts@biomass-derived porous carbon. The biological fungus realizes the formation of highly-porous graphene-like carbon, which constructs the 3D framework for high-potential polyanions. The polyanion nanocrystals are closely enwrapped by the biomass-derived framework and build the hybrid architecture. Both the highly-conductive skeleton and the hierarchically porous architecture of hybrid foams are favourable to highly-efficient electron and ion transport. Moreover, the depressed structural deterioration rate and improved contact between active material and conductive substrate are achieved for the 3D hybrid foams than conventional electrodes through dynamic studies. Without additional additive or binders, the freestanding hybrid foams achieve desirable characteristics of high operating potentials, fast sodium intercalation and excellent cycling stability. The $\text{Na}_7\text{V}_4(\text{P}_2\text{O}_7)_4(\text{PO}_4)$ - and $\text{Na}_7\text{V}_3(\text{P}_2\text{O}_7)_4$ -based hybrid foams retain respectively 94% and 91% of the capacities after 800 cycles at alternative 20 C and 3 C, demonstrating their superior high-rate ultralong-term cycling capability. Therefore, this study provides a low-cost, highly efficient and wide applicable architecture to construct high-potential and ultralong-life cathodes for sodium batteries.

1 Introduction

Sodium ion batteries with low-cost and abundant raw materials have attracted great attentions, particularly for large-scale and price-sensitive applications such as electric grids energy storage systems. However, the larger radius of sodium than lithium leads to low ion insertion reversibility, inferior kinetics and phase instability of the sodium hosts in comparison to the lithium counterparts.^{1,2} Therefore, designing high-performance sodium hosts, especially those for cathodes, with high-potential, fast kinetics and good stability is crucial to realize the full potential of SIBs. Among present sodium hosts, polyanion-based materials are promising candidates. Many polyanion sodium hosts including phosphates (e.g. $\text{Na}_3\text{V}_2(\text{PO}_4)_3$, NaFePO_4 , $\text{Na}_3\text{Ti}_2(\text{PO}_4)_3$, etc)³⁻⁶ pyrophosphates ($\text{Na}_2\text{FeP}_2\text{O}_7$, NaVOPO_4 , $\text{Na}_{4-x}\text{Fe}_{2+x/2}(\text{P}_2\text{O}_7)_2$, $\text{Na}_2(\text{VO})\text{P}_2\text{O}_7$, $\text{Na}_7\text{V}_3(\text{P}_2\text{O}_7)_4$, etc),^{7-12,26} fluorophosphates (NaVPO_4F , $\text{Na}_2\text{FePO}_4\text{F}$, $\text{Na}_3\text{V}_2(\text{PO}_4)_2\text{F}_3$, etc),^{13,14} sulfates ($\text{Na}_2\text{Fe}(\text{SO}_4)_2 \cdot 2\text{H}_2\text{O}$, $\text{Na}_{2+2x}\text{Fe}_{2-x}(\text{SO}_4)_3$),¹⁵⁻¹⁹ and mixed-polyanions (e.g. $\text{Na}_7\text{V}_3(\text{P}_2\text{O}_7)_4(\text{PO}_4)$, $\text{Na}_4\text{Fe}_3(\text{PO}_4)_2(\text{P}_2\text{O}_7)$, $\text{Na}_3\text{FeCO}_3\text{PO}_4$), et al.)²⁰⁻²⁵ have been extensively investigated as sodium hosts.

Among these polyanion-based materials, the nearest neighbors of two vanadium-based composites, i.e. $\text{Na}_7\text{V}_4(\text{P}_2\text{O}_7)_4(\text{PO}_4)$ and $\text{Na}_7\text{V}_3(\text{P}_2\text{O}_7)_4$, have attracted great

attention.^{11,21-23,26-28} As illustrated in Figure 1a, both composites have high-operating potentials (near 4.0 V vs. Na^+/Na) and facile sodium intercalation channels. For example, the framework of $\text{Na}_7\text{V}_4(\text{P}_2\text{O}_7)_4(\text{PO}_4)$ (Figure 1c) is constructed by PO_4 tetrahedron sharing corners with four adjacent VO_6 octahedrons and P_2O_7 group sharing corners with two adjacent VO_6 octahedrons.²¹⁻²³ Sodium ions at three different interstitial sites diffuse along the well-defined open channels. On the other hand, the basic unit of $\text{Na}_7\text{V}_3(\text{P}_2\text{O}_7)_4$ (Figure 1b) is constructed by VO_6 octahedral sharing corners with P_2O_7 diphosphate groups.^{11,26-28} Two parallel subunits coexist and construct a quasi two-dimensional network. Sodium ions at four different sites diffuse along the fast ion-conducting planes. Therefore, both sodium vanadium polyanions have well-defined framework as well as facile ion diffusion channels and high operating potential, which make them promising cathode candidates for sodium ion battery. However, problems such as poor conductivity, limited ion intercalation kinetic and inferior stability, greatly restricted their practical application. Therefore, further improvements on high-rate capability and long-term cycling performance are still big challenges for both high-potential sodium hosts.

Three-dimensional (3D) porous foam show great superiority in energy storage applications.²⁹⁻³⁸ Its abundant interconnected voids offer sufficient contact area between the electrolyte and

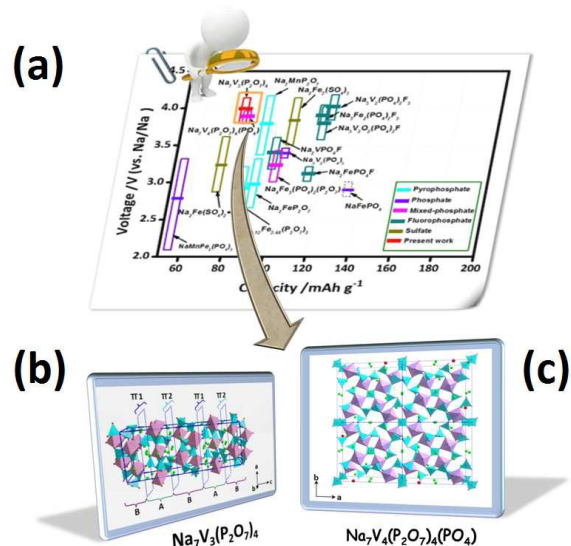


Figure 1 (a) Operating potentials and (b, c) crystal structures of $\text{Na}_7\text{V}_4(\text{P}_2\text{O}_7)_4(\text{PO}_4)$ (b) and $\text{Na}_7\text{V}_3(\text{P}_2\text{O}_7)_4$ (c). Operating potentials of other typical reported polyanion materials for sodium ion batteries are illustrated.

electrode, resulting in the fast electron/ion transport and shorten the solid-state ion diffusion paths. Moreover, the hierarchical porosity alleviates the structure deterioration during ion de/intercalation and improves cycling stability. All these advantages promote the application of 3D foam on electrode materials. Recently, intensive efforts have been devoted to construct 3D foam for energy storage devices. Many materials such as metal/alloy (e.g. Ni foam, Cu foams),^{29,30} simple inorganic composites (e.g. graphene foam, Si/graphene foam),³¹⁻³³ metal oxides (e.g. $\text{Fe}_3\text{O}_4/\text{graphene}$ foam, Co_3O_4 foam),^{34,35} metal sulfates (e.g. $\text{MoS}_2/\text{graphene}$ foam),^{36,37} simple phosphates (e.g. $\text{A}_3\text{V}_2(\text{PO}_4)_3/\text{C}$ foam)³⁸ etc, have been successfully constructed. However, most present studies in this field focus on simple materials with less elements (or groups) and simple structures. The application of 3D foam architecture on more complex materials with more elements (or groups) and intricate compositions, such as mixed-polyanions or multi-polyanions, are still challenging and remains largely unexplored. Therefore, it is crucial to develop advanced electrodes of complex polyanions through designing and constructing 3D foam architecture. Moreover, it is especially urgent for those with high operating potential in sodium intercalation systems, which have intrinsically slow kinetics and phase instability than lithium systems.

Following this viewpoint, for the first time, we construct freestanding 3D hybrid foams of high-potential mixed-polyanions (multi-polyanions) @ biomass-derived porous carbon. Two high-potential materials, i.e. $\text{Na}_7\text{V}_4(\text{P}_2\text{O}_7)_4(\text{PO}_4)$ and $\text{Na}_7\text{V}_3(\text{P}_2\text{O}_7)_4$, are employed as active components. The porous bio-carbon sponge was derived from natural-biomass of fungus (Figure 2a). As a large group of eukaryotic organisms, the fungus has been widely applied in food and pharmaceutical industries.³⁹ The fast growth rate and easy cultivation make it a world-wide abundance natural

resource.⁴⁰ As illustrated in Figure 2b, the nanocrystals of polyanions are closely anchored on biomass-derived carbon framework and construct the 3D hybrid foams. The highly-conductive framework facilitates fast electron transport, and the hierarchical porous structure enables efficient ion transport. Moreover, the layered-stacking bio-carbon offers improved volume density than popular carbons such as graphene nanomesh, porous graphene, activated carbon and carbon nanotube, and makes up for the fatal defect of porous architecture in electrochemical storage devices.⁴¹

As applied in sodium ion system, the 3D hybrid foam exhibits favorable high-potential, excellent high-rate capability and stable ultralong-term cycling property. The results demonstrate its superiority in energy storage systems. As a proof-of-concept study, the present biomass-based 3D hybrid foams provide a low-cost and highly-efficient strategy to fabricate high-performance electrodes for advanced sodium ion batteries.

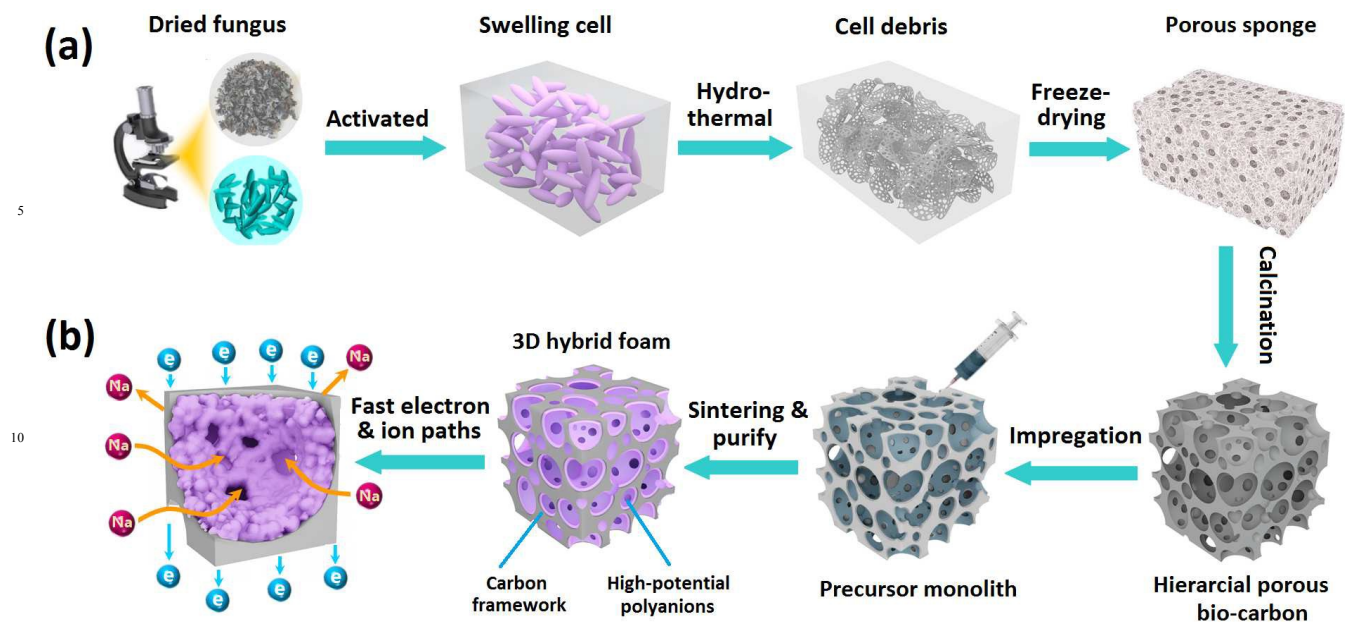
2 Experimental

2.1 Synthesis

Preparation of porous bio-carbon monolith. The dried fungus (*Auricularia*) were washed in the deionized water to remove unwanted impurities and then dried at 45 °C for a week before use. In a typical synthesis, 2 g purified dried fungus were added to 25 ml potassium hydroxide solution. Then the mixture was sealed in an autoclave and heated at 110 °C for 24 hours. After cooled down to room temperature, the obtained suspension was washed and put into the desirable shaped vessels. Then they were frozen in liquid nitrogen for 24 hours, followed by the vacuum drying process for two days in a freeze-drying machine. After that, the obtained monolith were taken out and calcinated at 800 °C for two hours in Ar atmosphere. Finally, the products were washed until pH value of filtrate reaches 7.

Preparation of $\text{Na}_7\text{V}_4(\text{P}_2\text{O}_7)_4(\text{PO}_4)$ and $\text{Na}_7\text{V}_3(\text{P}_2\text{O}_7)_4$ precursor. The starting materials of NH_4VO_3 , NaHCO_3 and $\text{NH}_4\text{H}_2\text{PO}_4$ with different ratios were mixed to form a homogenous solution, and then the citric acid was added into above solution. The mixture was kept at 80 °C for 20 hours under magnetic stirring. Then obtained transparent concentrate solutions were used as the precursor solutions of $\text{Na}_7\text{V}_4(\text{P}_2\text{O}_7)_4(\text{PO}_4)$ and $\text{Na}_7\text{V}_3(\text{P}_2\text{O}_7)_4$.

Construction of $\text{Na}_7\text{V}_4(\text{P}_2\text{O}_7)_4(\text{PO}_4)$ and $\text{Na}_7\text{V}_3(\text{P}_2\text{O}_7)_4$ hybrid foams @ 3D bio-carbon. The 3D hybrid foams were constructed by a preform impregnation process carried out in a lab-assembled system. Firstly, the bio-carbon monolith was placed in the sealed glass vessel. Then precursor solutions of $\text{Na}_7\text{V}_4(\text{P}_2\text{O}_7)_4(\text{PO}_4)$ and $\text{Na}_7\text{V}_3(\text{P}_2\text{O}_7)_4$ were slowly dropped into the porous bio-carbon skeleton with vacuum in between to ensure the effective impregnation. The whole impregnation system was kept at 80 °C to enable slowly drying of the mixture. After impregnation process, the intermediate product was annealed at respectively 850 °C and 650 °C respectively for 10 hours in Ar atmosphere to obtain the $\text{Na}_7\text{V}_4(\text{P}_2\text{O}_7)_4(\text{PO}_4)$ and $\text{Na}_7\text{V}_3(\text{P}_2\text{O}_7)_4$ -based intermediate products. After purification, the target 3D hybrid foams were obtained.



15 Figure 2 Schema of the synthetic approach of (a) porous biomass-derived carbon sponge and (b) freestanding 3D hybrid foams. (a) Activation, hydrothermal, freeze-drying and calcination procedures for preparing porous carbon monolith from natural fungus; (b) Fabrication of 3D hybrid foams through impregnation process. Partially enlarged image emphasizes the polyanion crystals anchored on the porous framework. The highly efficient electron/ion transport pathways are illustrated.

20 **Preparation of reference samples.** For comparison, the reference samples were prepared *via* conventional solid-state synthesis. Starting materials of V_2O_5 , Na_2CO_3 , $NH_4H_2PO_4$ and glucose were dispersed in alcohol and then ball milled by a planetary high-energy ball mill for 10 hours. After the evaporation of alcohol, the solid mixture of $Na_7V_4(P_2O_7)_4(PO_4)$ and $Na_7V_3(P_2O_7)_4$ were sintered at 850 °C and 650 °C for 12 hours in Ar atmosphere. Finally, the reference samples were obtained after purification of the calcination products.

2.2 Materials characterization

30 Powder X-ray diffraction (XRD, Bruker D8/Germany) using $Cu\ K\alpha$ radiation was employed to identify the crystalline phase of the material. *Ex-situ* XRD patterns were carried out on the electrodes before and after cycles, which were fixed in a lab-assembled aluminum-container. The morphology was observed with a scanning electron microscope (SEM, HITACHIS-4700) and a transmission electron microscope (TEM, JEOS-2010 PHILIPS). Raman spectra were recorded with a Labram HR-800 (HORIBA JobinYvon) spectrometer. Nitrogen adsorption-desorption isotherms were measured using a Micromeritics ASAP 2010 sorptometer. Carbon contents of the samples were determined by an element analyzer (EA, Elementar Vario EL).

2.3 Electrochemical measurements

40 The electrochemical characteristics were measured in CR2032 coin cells. The coin cells were assembled in an argon filled glove box. The 3D freestanding hybrid foams are directly used as electrode without additional components such as binder, conductive additive or current collector. The reference electrode are made in a traditional way. The mixture of the reference

material, carbon black and polyvinylidene fluoride (PVDF) in a weight ratio of 8:1:1. Then it was mixed with a minimal amount of N-methylpyrrolidone (NMP) solvent and the slurry was pasted on an aluminum-foil. The as-prepared electrode sheet was dried at 80 °C under vacuum overnight. Na foil as counter and reference electrode and $1\ mol\cdot L^{-1}\ NaClO_4$ dissolved in propylene carbonate (PC) was used as electrolyte. Galvanostatic charge-discharge tests were performed on a Land battery testing system (Wuhan, China). EIS measurements were conducted using a Zivelab electrochemical workstation, and the applied frequency range is 100k~1 mHz.

3 Results and Discussion

50 The construction of 3D hybrid foams of sodium vanadium polyanions@bio-carbon proceeds along a perform impregnation process. As illustrated in Figure 2a, the porous monolithic bio-carbon is prepared from natural fungus. The rich chitin, abundant microchannels and volumetric swelling properties enable fungus a good carbon precursor (Figure 3a).³⁹⁻⁴¹ In order to prevent cell-walls agglomeration, KOH solution is introduced into the bio-cell firstly. Then the lignin and semicellulose in the cell-walls are partially hydrolyzed in the hydrothermal process, and the swelling cells are severely broken. As a result, lots of debris of cell-walls with abundant voids is produced. The debris accumulates layer by layer during freeze-drying and constructs the bio-carbon monolith (Figure 3b). After calcination, the biomass-derived carbon sponge with porous carbon nanosheets is successfully constructed (Figure 3c and d). The element analysis results demonstrate that the main composition of the sponge are C and O, while content of K

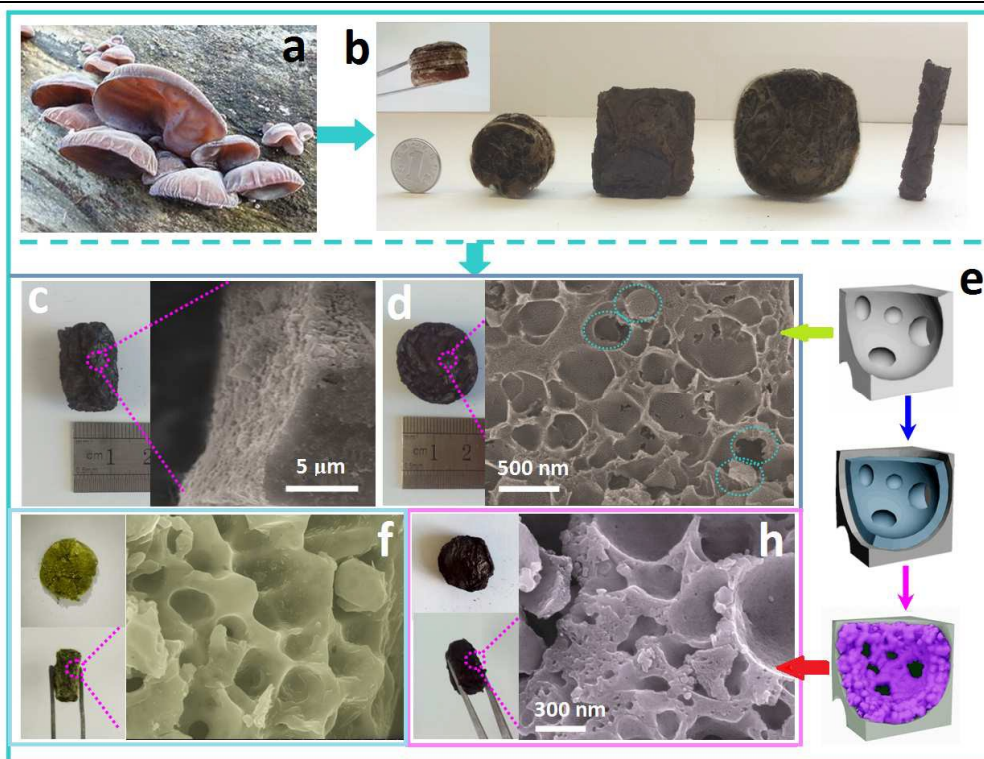


Figure 3 Photos of (a) natural fungus and (b) bio-carbon sponges in different geometries. (c, d, f, h) Photos and SEM images of the bio-carbon framework (c, d), intermediate monolith after impregnation (f) and 3D hybrid foams (h). (e) Schema of the architecture variation during impregnation process. Top model: bio-carbon framework; middle model: intermediate monolith; down model: hybrid foam. In d, the dotted curves show the peeled carbon nanosheets and the place where the sheets are peeled from.

20 element is extreme low (≤ 1 wt.%) and almost undetectable. The impregnation process is carried out based on the prepared bio-carbon monoliths. As illustrated in Figure 2b and 3e, the concentrated solutions of both sodium polyanions are respectively vacuum infiltrated into the carbon sponge. To ensure
 25 sufficient solution impregnation, such conditions as slowly speed, strong vacuum and simultaneous drying, are carefully controlled. As displayed in Figure 3f and e (middle model), the carbon framework is uniformly wrapped by the polyanion precursors after impregnation and the 3D hybrid precursors are constructed.
 30 Finally, after calcination and purification process, the target 3D hybrid foams of sodium vanadium polyanions@bio-carbon are fabricated (Figure 3h and down model of e).

The morphology and microstructure of prepared 3D hybrid foams were further investigated by TEM observations. As
 35 displayed in Figure 4a, the material exhibits a 3D cellular framework on large microscaled scale. The low-resolution images (Figure 4b, c) indicate the existence of nanocrystals in the size of 20–40 nm, which distribute on the framework of bio-carbon monolith. The enlarged image (Figure 4g) demonstrate that the
 40 abundant macropores exist in the framework. Moreover, the interconnections between the macropores are also observed, which produce smaller mesopores and construct the hierarchical porous architecture (Figure 4f). The highly porous framework not only facilitates easy electrolyte penetration, but also enables fast
 45 ion transport. More detailed information is provided by the high-

65 resolution TEM observation and EDS element analysis. As displayed in Figure 4h, the well-resolved lattice fringe indicates the single-crystal nature of polyanion crystals. Moreover, the element mapping analysis reveal that all of the elements uniformly distribute in the whole range (Figure 4e),
 70 demonstrating its uniform composition. Similar structure is also obtained for the $\text{Na}_7\text{V}_3(\text{P}_2\text{O}_7)_4$ -based hybrid foam (Figure s1). Therefore, the above results demonstrate that 3D hybrid foams of sodium vanadium polyanion@bio-carbon with hierarchical porous architecture and uniform composition have been
 75 successfully constructed.

Raman spectroscopy is recorded to further characterize the nature of carbon in hybrid foams. As displayed in Figure 4d, two characteristic signatures located at ~ 1360 and 1590 cm^{-1} are observed for the composite, which correspond to the *D*
 80 (disordered carbon) and *G* (graphene carbon) bands.^{42,43} The high ratio of *G/D* band intensity indicates the higher amount of sp^2 -type carbon than the sp^3 -type one. The result demonstrates the high graphitization of biomass-derived carbon framework, which is favorable to enhancing the electrical conductivity of hybrid
 85 foam. Therefore, as illustrated in Figure 2b, the highly-conductive graphene-like framework provides fast electron transport pathways, and the abundant hierarchical pores enable fast ion transport. Both advantages are favorable to sodium intercalation chemistry and reversible electrochemical property of
 90 sodium hosts.

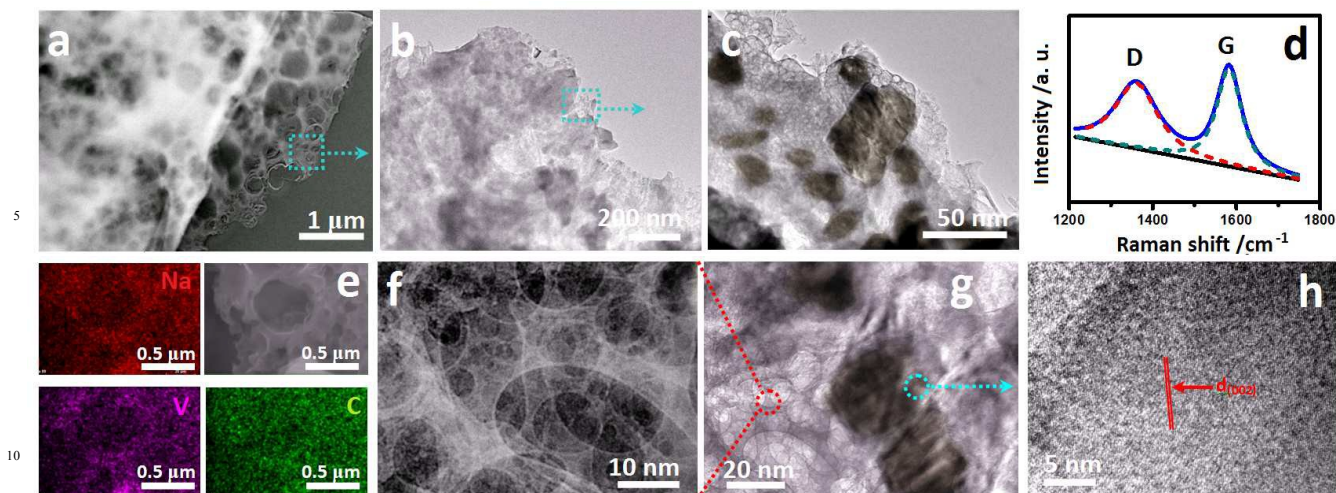


Figure 4 Morphologies and microstructures of the 3D hybrid foams: (a) Bright-field TEM image, (b, c) low resolution images, (e) EDS element mapping and (d) Raman spectroscopy of the 3D $\text{Na}_7\text{V}_4(\text{P}_2\text{O}_7)_4(\text{PO}_4)$ -based hybrid foam; (g) Enlarged image emphasized one crystal enveloped by the porous carbon; (f, h) HRTEM images of the hierarchical porous carbon network (f) and the polyanion nanocrystal (h) partially enlarged from g. In h, the arrow shows the lattice fringe corresponding to the (002) lattice plane of the $\text{Na}_7\text{V}_4(\text{P}_2\text{O}_7)_4(\text{PO}_4)$ crystal.

The carbon contents of the $\text{Na}_7\text{V}_4(\text{P}_2\text{O}_7)_4(\text{PO}_4)$ and $\text{Na}_7\text{V}_3(\text{P}_2\text{O}_7)_4$ hybrid foams are 6.5% and 6.9% respectively. Because introduce too much carbon will decrease the overall capacity of the cathodes, the possible methods to control the carbon content of hybrid foams are discussed. One possible strategy is based on the adjustment of impregnation conditions. Decreasing the solution dropping speed and increasing the system temperature will accelerate the drying speed of precursor solution. Thus more active material will be attached on the carbon framework and the carbon content will decrease. The other possible strategy is the optimization of carbon framework. Thus the weight ratio of carbon framework as well as the carbon content will decrease. It is beneficial to decrease the weight ratio of carbon framework in the hybrid foam and results in the decreased carbon content. Because of the importance of controlling carbon content for the freestanding carbon-based materials, we will carry out further work on this subject.

The crystal structures of the hybrid foams are identified by X-ray diffraction (XRD). In order to clarify the advantage of 3D foam architecture, the reference samples are prepared *via* solid-state strategy. The morphology of the reference samples are displayed in Figure s2. The hybrid foams exhibit higher BET surface areas than the reference ones (Figure 5 c and d), demonstrating the superiority of highly porous architecture than the solid particles of reference samples. XRD patterns of the hybrid foams and reference samples are displayed in Figure 5(a, b) and s3. Moreover, Rietveld refinements were carried out to clarify the purity of the prepared hybrid foams. The low difference between the calculated and observed values certifies the satisfactory results of the refinements. As shown in Figure 5a, all the diffraction peaks of the $\text{Na}_7\text{V}_4(\text{P}_2\text{O}_7)_4(\text{PO}_4)$ -based composites can be indexed to the tetragonal phase with space group of $P-42_1c$. The lattice parameters obtained by the Rietveld

refinement are $a=14.2165(2)$ Å and $c=6.3768(4)$ Å ($R_p=5.51\%$, $R_{wp}=6.24\%$). On the other hand, the $\text{Na}_7\text{V}_3(\text{P}_2\text{O}_7)_4$ -based foam can be indexed to the monoclinic structure with $C2/c$ space group. The lattice parameters obtained by the Rietveld refinement are $a=9.5489(2)$ Å, $b=8.3813(4)$ Å, $c=27.7395(4)$ Å and $\beta=92.8(1)^\circ$ ($R_p=8.47\%$, $R_{wp}=10.11\%$). The absence of impurity phase indicates the high purity of all the materials. The uneven backgrounds at $20^\circ\sim 40^\circ$ are observed for the hybrid foams, which correspond to their bio-carbon based framework. Moreover, the element analysis results demonstrate that element composition of all the samples coincide with the designed values (Table s1). Therefore, the results demonstrate that 3D hybrid foams with desirable crystal structure and element composition have been constructed.

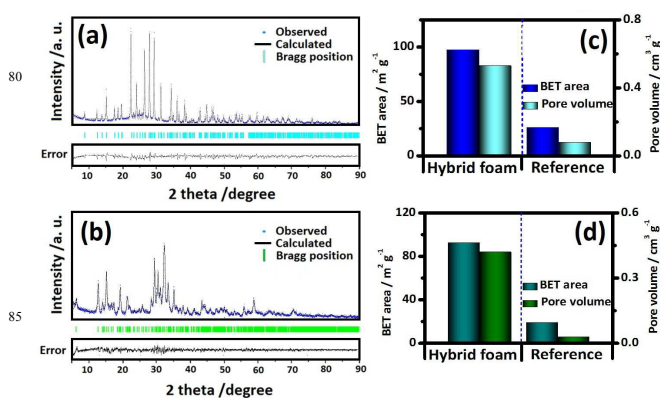


Figure 5 (a, b) XRD patterns of (a) $\text{Na}_7\text{V}_4(\text{P}_2\text{O}_7)_4(\text{PO}_4)$ - and (b) $\text{Na}_7\text{V}_3(\text{P}_2\text{O}_7)_4$ -based 3D hybrid foams and their refinement results. (c, d) Comparisons of the BET areas and pore volumes between (c) $\text{Na}_7\text{V}_4(\text{P}_2\text{O}_7)_4(\text{PO}_4)$ - and (d) $\text{Na}_7\text{V}_3(\text{P}_2\text{O}_7)_4$ -based hybrid foams and reference samples.

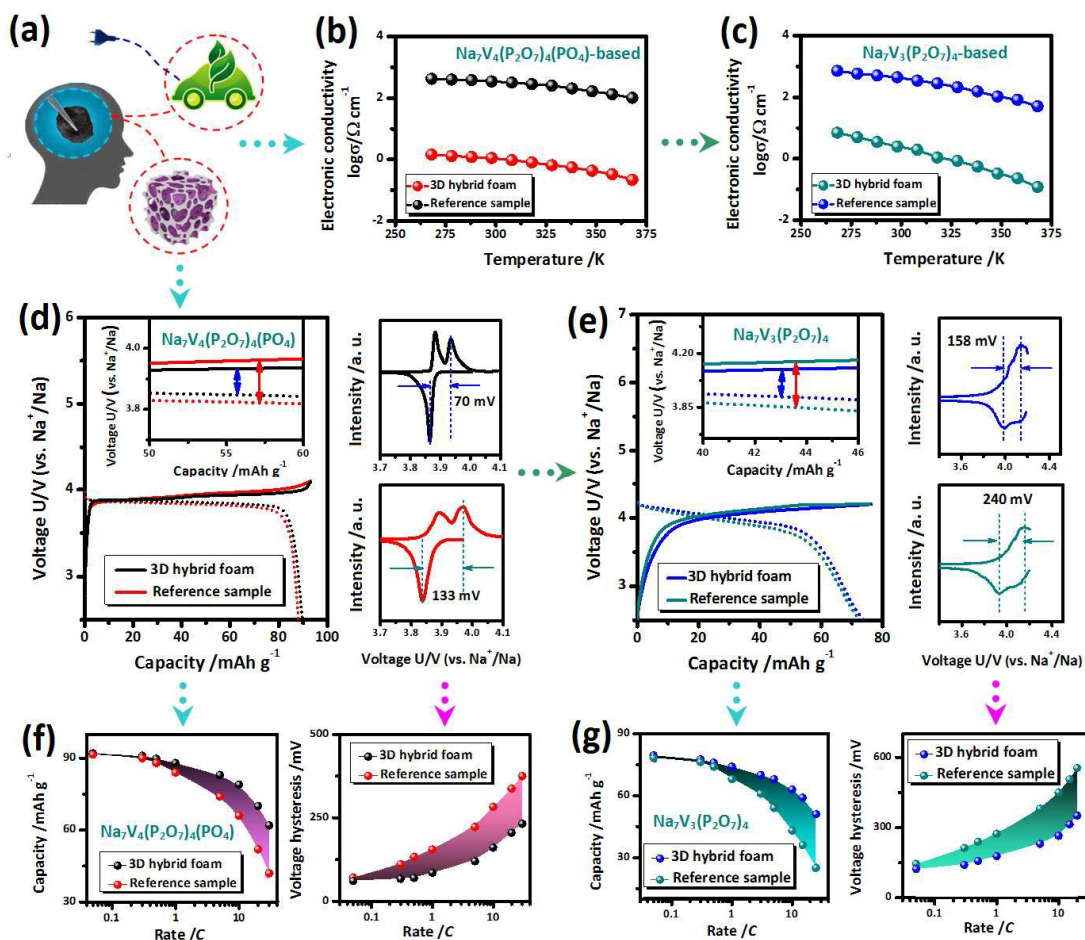


Figure 6 Electronic conductivity and galvanostatic charge/discharge characteristics of 3D hybrid foams: (a) Schema of designing high-performance electrode for practical applications such as electric vehicles; (b, c) Electronic conductivities of $\text{Na}_7\text{V}_4(\text{P}_2\text{O}_7)_4(\text{PO}_4)$ -based (b) and $\text{Na}_7\text{V}_3(\text{P}_2\text{O}_7)_4$ -based (c) hybrid foams and reference samples; (d, e) Typical galvanostatic charge/discharge curves (left) and differential capacity curves (right) of the $\text{Na}_7\text{V}_4(\text{P}_2\text{O}_7)_4(\text{PO}_4)$ -based (d) and $\text{Na}_7\text{V}_3(\text{P}_2\text{O}_7)_4$ -based (e) hybrid foams (up) and reference samples (down). The enlarged charge/discharge curve images are displayed as inserts of d and e; (f, g) Discharge capacities (left) and charge/discharge hysteresis (right) of the $\text{Na}_7\text{V}_4(\text{P}_2\text{O}_7)_4(\text{PO}_4)$ -based (f) and $\text{Na}_7\text{V}_3(\text{P}_2\text{O}_7)_4$ -based (g) hybrid foams and reference samples.

One major advantage of 3D freestanding architecture is their independent feature. It enables the formation of electrodes without additional binder or conductive, which is favorable to improving conductivity and facilitates practical applications. To clarify the superiority of 3D hybrid foams, we compare their electron conductivities with the pellets of reference ones. As displayed in Figure 6b and c, the electron conductivities of both hybrid foams are over two orders higher than the reference samples in the whole temperature range. The results demonstrate the highly efficient electron transfer capability of 3D hybrid foams.

More evidence on the superiority of hybrid foam is derived from galvanostatic charge/discharge results. As displayed in Figure 6d and e, the $\text{Na}_7\text{V}_4(\text{P}_2\text{O}_7)_4(\text{PO}_4)$ and $\text{Na}_7\text{V}_3(\text{P}_2\text{O}_7)_4$ based composites exhibit operating potentials near to 4.0 V vs. Na^+/Na , demonstrating their excellent high-potential characteristics. Although the electrodes in different architectures display similar charge capacities at 0.5 C, the discharge capacities and coulombic

efficiencies of 3D hybrid foams are higher than those of the reference ones. Moreover, great difference is observed in their hysteresis between the charge/discharge curves. As compared in Figure 6d and e, both the charge/discharge curves and differential capacity curves demonstrate that various structured electrodes have different charge/discharge hysteresis. For example, the hysteresis of $\text{Na}_7\text{V}_4(\text{P}_2\text{O}_7)_4(\text{PO}_4)$ and $\text{Na}_7\text{V}_3(\text{P}_2\text{O}_7)_4$ -based hybrid foams are only half or two thirds than those of the reference ones. Figure 6f and g summarize the change of discharge capacity and charge/discharge hysteresis of all the samples at different current densities. As the current density is increased, the differences of both discharge capacity and charge/discharge hysteresis between 3D hybrid foams and reference samples increase correspondingly. The results indicate that the hybrid foams have better electrochemical reversibility and faster kinetics than conventional electrodes. As illustrated in Figure 6a and 2b, the improvement can be attributed to the unique architecture of 3D hybrid foam, which provides lower electron-transfer resistivity and higher

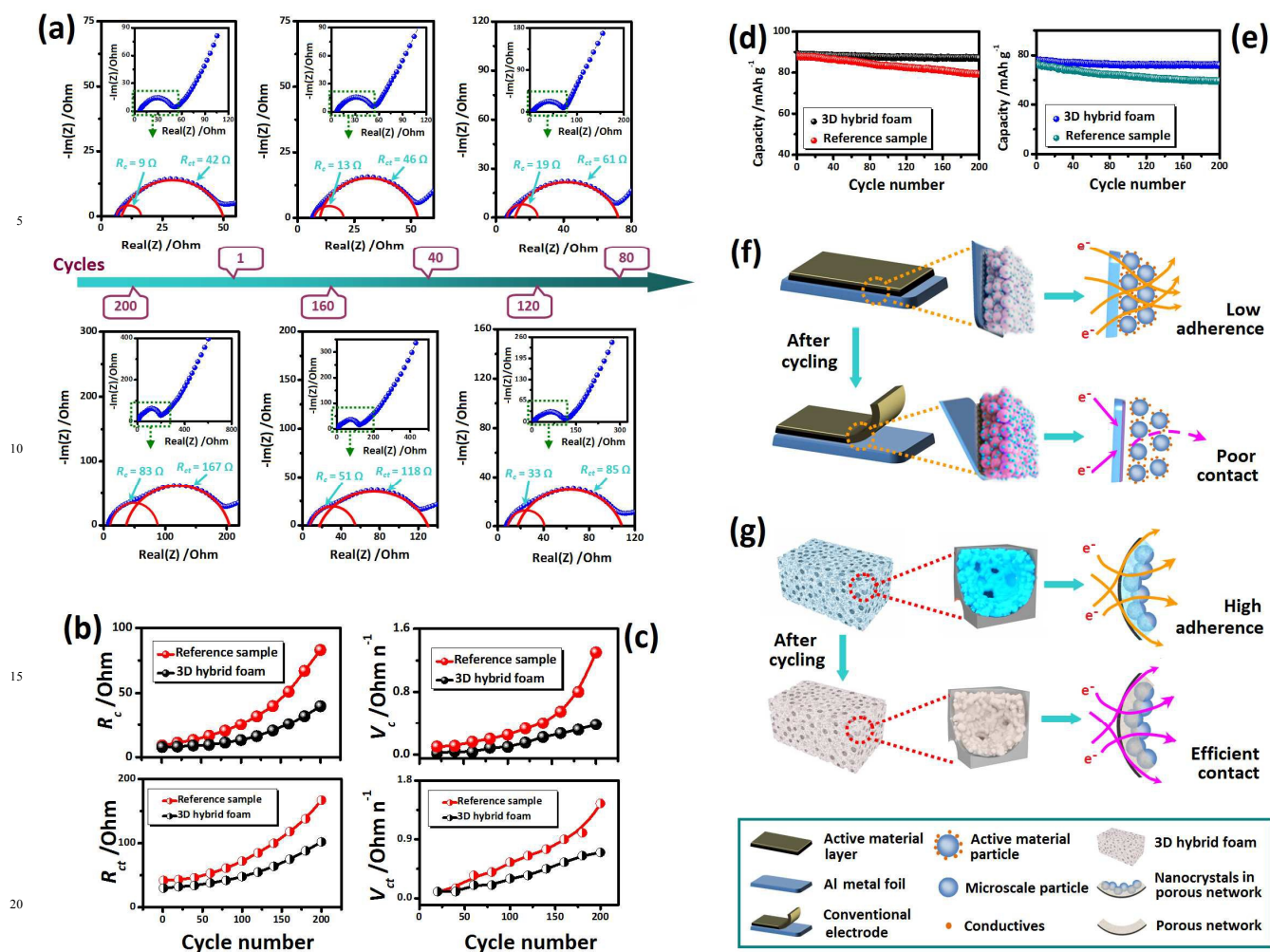


Figure 7 Dynamic studies of the deterioration mechanism in different architecture electrodes: (a) Nyquist plots of $\text{Na}_7\text{V}_4(\text{P}_2\text{O}_7)_4(\text{PO}_4)$ -based reference electrodes after different cycles; (b) The relationship between the contact resistance (R_c : up) and charge transfer resistance (R_{ct} : down) and the cycle numbers; (c) The relationship between the deterioration rates of v_c (up) and v_{ct} (down) and the cycle numbers; (d, e) Cycling properties of the $\text{Na}_7\text{V}_4(\text{P}_2\text{O}_7)_4(\text{PO}_4)$ -based (d) and $\text{Na}_7\text{V}_3(\text{P}_2\text{O}_7)_4$ -based (e) composites in different architectures at 0.5 C; Schema of the deterioration process for the conventional electrode (f) and 3D hybrid foam (g) during cycling.

active surface area between the electrolyte and electrode. Therefore, all above results demonstrate the superior electron transport capability and good electrochemical reversibility of 3D hybrid foams, which are favorable to their cycling property.

As employed in practical applications, the cycling properties, especially the high-rate long-term cycling properties, are important criterions for the electrodes. Therefore, we investigated the cycling performances of all the samples. Firstly, the low-rate cycling performance at 0.5 C is studied. As displayed in Figure 7d and e, the hybrid foams exhibit better cycling property than the reference ones. For example, the $\text{Na}_7\text{V}_4(\text{P}_2\text{O}_7)_4(\text{PO}_4)$ -based hybrid foam achieves the capacity retentions of 98% after cycles at 0.5 C, but only 91% of the capacity is retained for the reference sample. Similarly, the $\text{Na}_7\text{V}_3(\text{P}_2\text{O}_7)_4$ hybrid foam retains 95% of the initial capacity after cycles, while only 82% of capacity remained for the reference sample after cycles.

To clarify the origin of enhanced cycling property of 3D hybrid foams, the electrochemical impedance spectroscopy (EIS) was carried out on all the electrodes after a certain cycles. Figure 7a illustrates the Nyquist plots of the $\text{Na}_7\text{V}_4(\text{P}_2\text{O}_7)_4(\text{PO}_4)$ -based reference electrode in conventional structure after different cycles. Three different signatures are observed in the EIS spectra, *i.e.* the high-frequency arc, the medium-frequency arc and the low-frequency line. The high-frequency arc is associated with the contact resistance (R_c) between the active materials and the conductive substrate; the medium-frequency arc can be explained as the charge-transfer resistance (R_{ct}); and the low-frequency straight line is an indicative of sodium solid-state diffusion capability inside the active material particles.^{32,44} As cycle number increases, the high-frequency and low-frequency arcs of the cycled electrodes initially are stable, and then slowly increase, and finally quickly jump up. The results demonstrate that the changing fashion of both R_c and R_{ct} values with the alteration of cycling number aren't uniform over the whole range.

Figure 7b summarizes the charge transfer resistances (R_{ct}) and contact resistances (R_c) of the samples during cycles. The 3D hybrid foam exhibit much lower R_{ct} and R_c values than the reference one, suggesting its improved contact and depressed deterioration during cycling. Moreover, the differences between the 3D hybrid foams and reference samples become larger as increasing the cycle numbers. In order to clarify the effect of different architecture, the apparent deterioration rates are calculated to characterize the deterioration process based on the following equations:

$$v_c = dR_c / dn \quad (1)$$

$$v_{ct} = dR_{ct} / dn \quad (2)$$

where v_c and v_{ct} are the apparent deterioration rates of active material/conductive substrate contact and the charge transfer capability; R_c and R_{ct} are contact resistance and charge transfer resistance at certain cycle; n is the cycle number.

Figure 7c displays the relationship between the apparent deterioration rates and the cycle numbers. For all the samples, when the cycle number is increased, the apparent deterioration rates of v_c and v_{ct} initially slowly increase, and then quickly increase. The enhanced deterioration rates with increasing cycle numbers indicate that the prior destroyed architecture will accelerate the following deterioration rate of the electrode. The results demonstrate that the contact between active material and conductive substrate turns even worse during cycles. The insufficient contact destroys electron transport pathways and is harmful to the sodium migration, which leads to fast deterioration of the electrochemical performance.

The slow deterioration rates of 3D hybrid foams demonstrate its superiority over the conventional structured electrodes. As illustrated in Figure 7f, for the reference samples, the large microsized particles are bound with conductive particles (e.g. activated carbon) and low-conductive binders (e.g. PVDF), which spreads on the metal-based substrate (e.g. Al foil) in low mechanical strength. It is easy to lose adherence and departure from the metal-based substrate because of possible side reactions such as passivation and/or corrosion of metal substrate, electrolyte decomposition and so on. Especially, the deterioration is even severe at high potentials. The insufficient contact makes fast increased contact resistance and decreased sodium transfer capability, which lead to poor cycling property of conventional electrodes. On the other hand, for the 3D hybrid foams (Figure 7g), the nanocrystals are closely enwrapped by the 3D porous framework, which provides good adherence between the active material and the 3D highly-conductive substrate. The excellent stability of highly-conductive carbon-based substrate facilitates the sodium de/intercalation for the high-potential polyanions. Moreover, the hierarchical porous architecture also acts as a buffer layer for the nanocrystals during ion de/intercalation, which is favorable to its cycling stability. Therefore, the 3D hybrid foam facilitates the good contact and suppresses the deterioration, which is beneficial to its high-rate capability and long-term cycling stability.

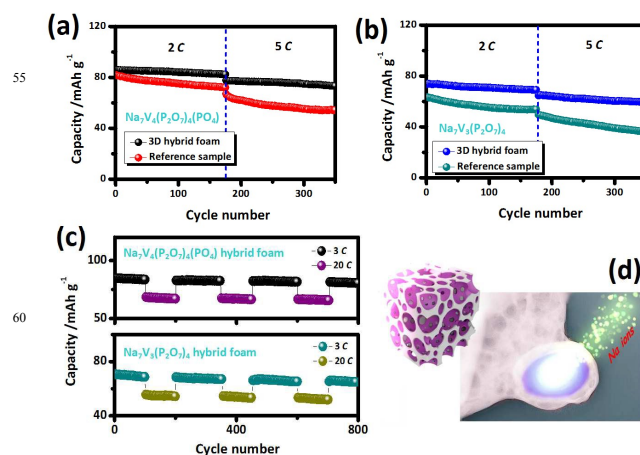


Figure 8 High-rate cycling property of the Na₇V₄(P₂O₇)₄(PO₄)-based (a) and Na₇V₃(P₂O₇)₄-based (b) hybrid foams and reference samples at 2 C and 5 C rates. (c) Ultralong-term cycling performance of the Na₇V₄(P₂O₇)₄(PO₄)-based (up) and Na₇V₃(P₂O₇)₄-based (down) hybrid foams at alternatively 3 and 20 C. (d) Schema of the hierarchical porous architecture and fast sodium ion pathways of the 3D hybrid foams.

Encouraged by the superior sodium intercalation kinetics, the high-rate long-term properties of the 3D hybrid foams are studied. As displayed in Figure 8a, the Na₇V₄(P₂O₇)₄(PO₄)-based 3D hybrid foam achieves the capacity retentions of 96% and 95% after cycles at 2 C and 5 C, respectively. On the contrary, the reference sample only obtains the capacity retentions of 88% at 2 C and 79% at 5 C. Similarly, the Na₇V₃(P₂O₇)₄ hybrid foam retains 94% and 92% of the initial capacity after cycles at 2 C and 5 C respectively, while only 85% (2 C) and 74% (5 C) of the capacity remained for the reference sample after cycles (Figure 8b).

To clarify the origin of the superiority of 3D hybrid foams, the structures of the samples after cycles are investigated. Figure 9(b, c, e, f) compare the *ex-situ* XRD patterns of all the samples before and after cycling. For all the samples, the materials after cycling exhibit lower peaks intensities than the ones before cycles, certifying their decreased crystallinity during cycling. Similar phenomenon has also been observed in many electrochemical active materials, which indicates the existence of structure deterioration during repeated ion deinter/intercalation.⁴⁵⁻⁴⁸ Moreover, the reference samples (Figure 9c, f) exhibit greater differences between the original and cycled electrodes as compared to the 3D hybrid foams (Figure 9b, e), indicating their faster and severer structure deterioration. On the other hand, the *ex-situ* XRD patterns of the cycled electrodes for both polyanions are compared in Figure 9a and d. The higher intensities of 3D hybrid foam than the corresponding reference one demonstrate its depressed structural deterioration and better cycling stability. Moreover, the EIS results of the cycled electrodes of both polyanions are compared in Figure 9g and h. The smaller contact resistance (R_c) and charge transfer resistance (R_{ct}) of the hybrid foam than those of the reference one further demonstrate their good contact and improved structure stability. Therefore, both

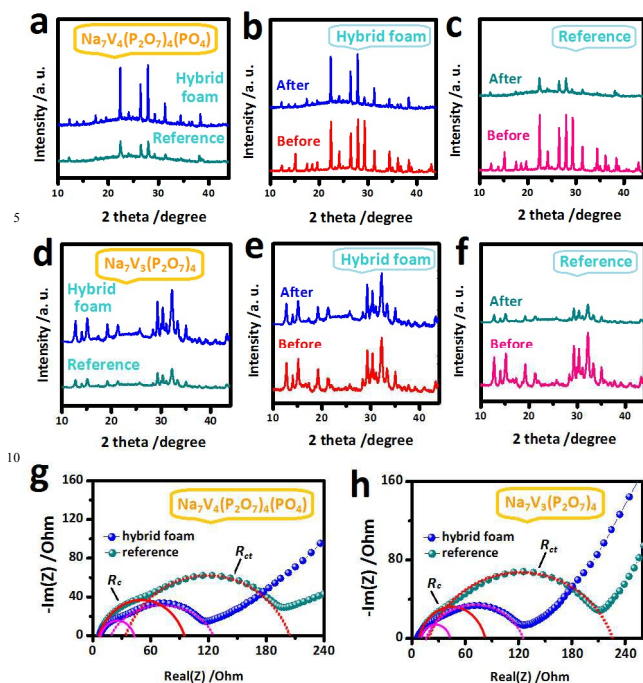


Figure 9 *Ex-situ* XRD patterns (a~f) and EIS results (g, h) of the $\text{Na}_7\text{V}_4(\text{P}_2\text{O}_7)_4(\text{PO}_4)$ -based (a~c, g) and $\text{Na}_7\text{V}_3(\text{P}_2\text{O}_7)_4$ -based (d~f, h) hybrid foams and reference electrode before and after cycles. Comparisons of *ex-situ* XRD patterns (b, c, e, f) of $\text{Na}_7\text{V}_4(\text{P}_2\text{O}_7)_4(\text{PO}_4)$ -based (b, c) and $\text{Na}_7\text{V}_3(\text{P}_2\text{O}_7)_4$ -based (e, f) hybrid foams (b, e) and reference electrodes (c, f) before and after cycles. Comparisons of *ex-situ* XRD patterns (a, d) and Nyquist plots (g, h) of the $\text{Na}_7\text{V}_4(\text{P}_2\text{O}_7)_4(\text{PO}_4)$ -based (a, g) and $\text{Na}_7\text{V}_3(\text{P}_2\text{O}_7)_4$ -based (d, h) hybrid foams and reference electrodes after cycles.

the *ex-situ* XRD and EIS results demonstrate the superior structural stability of the hybrid foams.

Moreover, the 3D hybrid foams are capable of ultralong-term cycling at high rates. As displayed in Figure 8c, the $\text{Na}_7\text{V}_4(\text{P}_2\text{O}_7)_4(\text{PO}_4)$ and $\text{Na}_7\text{V}_3(\text{P}_2\text{O}_7)_4$ -based hybrid foams retain 94% and 91% of the capacity after eight hundreds cycles alternatively at 20 C and 3 C. The results demonstrate the excellent high-rate ultralong-term cycling property of hybrid foams. It is associated with its unique architecture, which is favorable to fast electron/ion transport and good stability (Figure 8d). Combined above results, the advantages such as highly-conductive framework, hierarchical porosity, good stability and wide applicability make 3D hybrid foam a favorable architecture for high-potential electrodes. Therefore, the present study puts forwards a low-cost and highly-efficient strategy to construct cathode electrodes with high-potential and ultralong-life for advanced sodium ion batteries.

4 Conclusions

In summary, we have demonstrated the successful design and fabrication of a new architected electrode, named “freestanding 3D hybrid foam”, as a high-potential and ultralong-

life cathode for sodium ion batteries. The graphene-like skeleton is derived from the biological fungus, which constructs the 3D porous framework for high-potential sodium polyanions. The nanocrystals are closely wrapped by the highly conductive and highly porous framework, resulting in hierarchical hybrid architecture. Taking the advantage of hierarchical porosity, high conductivity and good stability, the 3D hybrid foams achieve fast sodium intercalation kinetics and superior cycling stability. As a proof-of-concept study, two typical high-potential sodium hosts, *i.e.* $\text{Na}_7\text{V}_4(\text{P}_2\text{O}_7)_4(\text{PO}_4)$ and $\text{Na}_7\text{V}_3(\text{P}_2\text{O}_7)_4$, are employed to construct hybrid foams in present study. The depressed structural deterioration and improved contact between active material and conductive substrate are demonstrated for the 3D hybrid foams compared to the conventional electrodes through dynamic studies. The hybrid foams achieve favorable high operating potentials and superior high-rate ultralong-term cycliling capability. The $\text{Na}_7\text{V}_4(\text{P}_2\text{O}_7)_4(\text{PO}_4)$ - and $\text{Na}_7\text{V}_3(\text{P}_2\text{O}_7)_4$ -based composites retains 94% and 91% of the capacities after 800 cycles at alternative rates of 20 C and 3 C. Therefore, the 3D hybrid foam is favorable to realizing superior electrochemical performance for high-potential polyanions, which puts forwards a significant step forwards the development of low-cost large-scale batteries.

Acknowledgements

This work is supported by the Natural Science Funds for Distinguished Young Scholar of Heilongjiang Province (No. JC2015001), Program for New Century Excellent Talents in Heilongjiang Provincial University (No. 1253-NCET-012) and Natural Science Foundation of Heilongjiang Province (No. QC2013C008).

Notes and references

^aKey Laboratory of Superlight Material and Surface Technology, Ministry of Education, College of Material Science and Chemical Engineering, Harbin Engineering University, Harbin 150001, Heilongjiang, China; E-Mail: senzhang@hrbeu.edu.cn

^bKey Laboratory for Photonic and Electronic Bandgap Materials, Ministry of Education; College of Chemistry and Chemical Engineering, Harbin Normal University, Harbin, 150025, Heilongjiang, China; E-Mail: chaodenghsd@sina.com

† Both authors contribute equally to this article.

†† Electronic Supplementary Information (ESI) available: Morphology and structure of the reference samples; Element analysis results of all the samples. See DOI: 10.1039/b000000x/

- 1 J. M. Tarascon, M. Armand, *Nature* **2001**, *4*, 359-367.
- 2 J. B. Goodenough, K. S. Park, *J. Am. Chem. Soc.* **2013**, *135*, 1167-1176.
- 3 Q. Y. Wang, B. D. Zhao, S. Zhang, X. H. Gao, C. Deng, *J. Mater. Chem. A* **2015**, *3*, 7732-7740.
- 4 B. D. Zhao, B. Lin, S. Zhang, C. Deng, *Nanoscale* **2015**, *7*, 18552-18560.
- 5 Z. L. Jian, Y. Sun, X. L. Ji, *Chem. Commun.* **2015**, *51*, 6381-6383.
- 6 B. D. Zhao, Q. Y. Wang, S. Zhang, C. Deng, *J. Mater. Chem. A* **2015**, *3*, 12089-12096.
- 7 P. Barpanda, G. D. Liu, C. D. Ling, M. Tamaru, M. Avdeev, S. C. Chung, Y. Yamada, *Chem. Mater.* **2013**, *25*, 3480-3487.

- 8 B. Lin, S. Zhang, C. Deng, *J. Mater. Chem. A* **2015**, *4*, 2550-2559.
- 9 P. Barpanda, S. Nishimura, A. Yamada, *Adv. Energy Mater.* **2012**, *2*, 841-859.
- 10 P. Barpanda, T. Ye, M. Avdeev, S. C. Chung, A. Yamada, *J. Mater. Chem. A*, **2013**, *1*, 4194-4197.
- 5 11 C. Deng, S. Zhang, B. D. Zhao, *Energy Storage Mater.* **2016**, DOI: 10.1016/j.ensm.2016.03.001
- 12 P. Barpanda, G. Liu, M. Avdeev, A. Yamada, *Chemelectrochem*, **2014**, *1*, 1488-1491.
- 10 13 Z. Liu, Y. Y. Hu, M. T. Dunstan, H. Huo, X. G. Hao, H. Zou, G. M. Zhong, Y. Yang, C. P. Grey, *Chem. Mater.* **2014**, *26*, 2513-2521.
- 14 W. X. Song, X. B. Ji, Z. P. Wu, Y. C. Yang, Z. Zhou, F. Q. Li, Q. Y. Chen, C. E. Banks, *J. Power Sources*, **2014**, *256*, 258-263.
- 15 15 P. Barpanda, G. Oyama, S. I. Nishimura, S. C. Chung, A. Yamada, *Nat. Commu.* **2014**, *5*, 4358.
- 16 Y. Meng, T. T. Yu, S. Zhang, C. Deng, *J. Mater. Chem. A* **2016**, *4*, 1624-1631.
- 17 P. Barpanda, G. Oyama, C. D. Ling, A. Yamada, *Chem. Mater.* **2014**, *26*, 1297-1299.
- 20 18 Y. Meng, S. Zhang, C. Deng, *J. Mater. Chem. A* **2015**, *3*, 4484-4492.
- 19 Y. Meng, Q. F. Li, T. T. Yu, S. Zhang, C. Deng, *CrystEngComm*, **2016**, *18*, 1645-1654.
- 25 20 S. Y. Lim, H. Kim, J. Chung, J. H. Lee, B. G. Kim, J. J. Choi, K. Y. Chung, W. Cho, S. J. Kim, W. A. Goddard, Y. S. Jung, J. W. Choi, *PNAS* **2014**, *111*, 599-604.
- 21 C. Deng, S. Zhang, *ACS Appl. Mater. Interfaces* **2014**, *6*, 9111-9117.
- 30 22 S. Zhang, C. Deng, Y. Meng, *J. Mater. Chem. A* **2014**, *2*, 20538-20544.
- 23 C. Deng, S. Zhang, Y. X. Wu, *Nanoscale* **2015**, *7*, 487-491.
- 24 H. Kim, I. Park, D. H. Seo, S. Lee, S. W. Kim, W. J. Kwon, Y. U. Park, C. S. Kim, S. Jeon, K. Kang, *J. Am. Chem. Soc.* **2012**, *134*, 10369-10372.
- 35 25 H. L. Chen, G. Hautier, G. Ceder, *J. Am. Chem. Soc.* **2012**, *134*, 19619-19627.
- 26 E. Quarez, O. Mentre, Y. Oumellal, C. Masquelier, *New J. Chem.*, **2009**, *33*, 998-1005.
- 40 27 C. Masquelier, F. D. Yvoire, *J. Solid State Chem.* **1991**, *95*, 156-167.
- 28 C. Masquelier, F. D. Yvoire, E. Bretey, P. Berthet, C. P. Chansac, *Solid State Ion.* **1994**, *67*, 183-189.
- 29 X. Xiao, P. Liu, J. S. Wang, M. W. Verbrugge, M. P. Balogh, *Electrochem. Commun.* **2011**, *13*, 209-212.
- 45 30 H. C. Shin, M. L. Liu, *Chem. Mater.* **2004**, *16*, 5460-5464.
- 31 B. Li, S. B. Yang, S. M. Li, B. Wang, J. H. Liu, *Adv. Energy Mater.* **2015**, *5*, 1500289.
- 32 H. X. Ji, L. L. Zhang, M. T. Pettes, H. F. Li, S. S. Chen, L. Shi, R. Piner, R. S. Ruoff, *Nano Lett.* **2012**, *12*, 2446-2451.
- 50 33 S. Nardecchia, D. Carriazo, M. Luisa Ferrer, M. C. Gutierrez, F. D. Monte, *Chem. Soc. Rev.* **2013**, *42*, 794-830.
- 34 Z. S. Wu, S. Yang, Y. Sun, K. Parvez, X. Feng, K. Mullen, *J. Am. Chem. Soc.* **2012**, *134*, 9082-9085.
- 55 35 Y. Q. Fan, H. B. Shao, J. M. Wang, L. Liu, J. Q. Zhang, C. N. Cao, *Chem. Commun.* **2011**, *47*, 3469-3471.
- 36 J. Wang, J. L. Liu, D. L. Chao, J. Yan, J. Y. Lin, Z. X. Shen, *Adv. Mater.* **2014**, *26*, 7162-7169.
- 37 W. J. Zhou, K. Zhou, D. M. Hou, X. J. Liu, G. Q. Li, Y. H. Sang, H. Liu, L. G. Li, S. W. Chen, *ACS Appl. Mater. Interfaces* **2014**, *6*, 21534-21540.
- 60 38 Y. P. Zhou, X. H. Rui, W. P. Sun, Z. C. Xu, Y. Zhou, W. J. Ng, Q. Y. Yan, E. Fong, *ACS Nano*, **2015**, *9*, 4628-4635.
- 39 L. Wei, M. Sevilla, A. B. Fuertes, R. Mokaya, G. Yushin, *Adv. Energy Mater.* **2011**, *1*, 356-361.
- 65 40 B. Hu, K. Wang, L. Wu, S. H. Yu, M. Antonietti, M. M. Titirici, *Adv. Mater.* **2010**, *22*, 813-828.
- 41 H. Zhu, X. L. Wang, F. Yang, X. R. Yang, *Adv. Mater.* **2011**, *23*, 2745-2748.
- 70 42 S. Zhang, C. Deng, H. Gao, F. L. Meng, M. Zhang, *Electrochim. Acta* **2013**, *107*, 406-412.
- 43 L. Tan, S. Zhang, C. Deng, *J. Power Sources* **2015**, *275*, 6-13.
- 44 D. Tu, B. Wu, B. Wang, C. Deng, Y. Gao, *Appl. Catal. B. Environ.* **2011**, *103*, 163-168.
- 75 45 M. Reynaud, G. Rousse, A. M. Abakumov, M. T. Sougrati, G. V. Tendeloo, J. N. Chotard, J. M. Tarascon, *J. Mater. Chem. A* **2014**, *2*, 2671-2680.
- 46 S. J. Lim, D. W. Han, D. H. Nam, K. S. Hong, J. Y. Eom, W. H. Ryu, H. S. Kwon, *J. Mater. Chem. A* **2014**, *2*, 19623-19632.
- 80 47 R. Dominko, M. Bele, A. Kokalj, M. Gaberscek, J. Jamnik, *J. Power Sources* **2007**, *174*, 457-461.
- 48 C. Deng, S. Zhang, *Nano Energy* **2014**, *4*, 49-55.